

Time delay interferometry with minimal null frequencies and shortened time span

Gang Wang^{1,*}

¹*Shanghai Astronomical Observatory, Chinese Academy of Sciences, Shanghai 200030, China*

(Dated: February 7, 2025)

In Paper I [1], we introduced an alternative second-generation time-delay interferometry (TDI) configuration, hybrid Relay, designed to minimize null frequencies and enhance data analysis for massive binary black hole (MBBH). In Paper II [2], we further improved its performance in noise characterization by replacing its null stream with a specialized stable channel, C_3^{12} . In this work, we propose a novel TDI configuration, labeled PD4L, which features minimal null frequencies and a reduced time span. Unlike the hybrid Relay or the second-generation Michelson, which require a maximum delay of $7L$ (where L is the ranging time of interferometric arm), the PD4L synthesizes data only within $3L$ delay. This shorter time span brings several advantages: 1) reducing margins at boundaries of data segments, 2) mitigating frequency aliasing in the high frequency band, and 3) shortening the tail at the end of a signal. To assess its effectiveness in data analysis, we perform parameter inference for a rapidly chirping gravitational wave signal from a MBBH. As a more compact TDI structure, PD4L achieves more accurate parameters estimation in the frequency-domain compared to the hybrid Relay. Additionally, PD4L's null stream exhibits minimal null frequencies, identical to its science channels, while maintaining a more stable noise spectrum than the C_3^{12} . We further evaluate its capability in noise characterization. The results demonstrate that although the stability of noise spectra in science channels is slightly lower compared to that of hybrid Relay, PD4L can still reliably infer noise parameters for data durations of up to four months. These investigations and comparisons suggest that PD4L is a promising TDI scheme, particularly for the higher frequency band.

I. INTRODUCTION

Time delay interferometry (TDI) was developed to suppress laser frequency noise and achieve the targeted sensitivity for space-borne interferometers [3–5]. It is essential for space missions such as LISA [6, 7], TAIJI [8], TianQian [9] to detect gravitational waves (GW) in the millihertz band. The principle of TDI is to combine interferometric laser links with appropriate delays to construct equivalent equal-arm interferometry. The first-generation TDI was formulated to cancel laser noise in a static unequal-arm case [4]. However, due to orbital dynamics, second-generation TDI is required to eliminate the effects of relative spacecraft (S/C) motions [10, 11].

The second-generation TDI configuration, Michelson, has been widely used as a benchmark for noise suppressions and data analysis. However, as we investigated in [1, 2], its performance degrades when transitioning from a static equal-arm scenario to a dynamic unequal-arm configuration. To address this, we proposed alternative TDI configuration, hybrid Relay, as a substitute to enhance the data analysis. One advantage of hybrid Relay is its minimal null frequencies, which contribute to greater stability in noise spectra. However, the hybrid Relay requires data to be delayed up to seven times the arm length, $7L$ (where L is the ranging time between S/C). As a result, TDI channels with longer time spans will introduce larger margins, leading to greater data loss at segment boundaries. Moreover, synthesizing interferometric data over an extended time span exacerbates fre-

quency aliasing in the high frequency band. To mitigate these disadvantages, a compact TDI configuration with a shorter time span is desirable.

In this work, we further investigate and compare a series of alternative TDI configurations developed in [12]. The objective is to identify a TDI configuration with minimized null frequencies and a shortened time span. We identify a promising TDI configuration, denoted as PD4L, which combines the first-generation TDI Monitor and Beacon. PD4L has a time span of $4L$ (with a maximum delay of $3L$) and features null frequencies that occur only at $f = m/L$, ($m = 1, 2, 3, \dots$) for both ordinary and optimal channels. As a second-generation TDI scheme, its time span is shorter than that of hybrid Relay or Michelson by $4L$. To evaluate its suitability, we conduct a multi-step assessment. First, we examine the stability of its noise spectra by calculating derivatives w.r.t. arm length variations. The results indicate that while the science channels of PD4L exhibit slightly lower robustness than those of hybrid Relay, it remains a viable candidate. An additional advantage of PD4L is that its null channel is more stable than C_3^{12} (which identified in [13]) and is the most stable null stream identified in our investigations so far. Second, we evaluate the sky-averaged GW response and sensitivity. Although PD4L's response function is weaker than that of hybrid Relay and Michelson in the lower frequency band, the sensitivities derived from its optimal channels are effectively identical. To further validate PD4L's performance, we simulate a rapidly chirping GW signal from a massive binary black hole (MBBH) and compute its responded waveforms in Michelson, hybrid Relay, and PD4L configuration. The results demonstrate that a TDI channel

* Gang Wang: gwanggw@gmail.com

with a shorter time span produces a smoother waveform. We also perform parameter inferences for the chirping signal in the frequency-domain. The findings suggest that PD4L achieves more reliable results for the high-frequency signals compared to the hybrid Relay. Finally, we conduct noise parameter characterizations using different durations, the results show that PD4L can accurately determine the parameter values over a 120-day data span.

This paper is organized as follows: In Section II, we introduce the second-generation TDI configurations considered in this study. Section III examines the noise spectra of the TDI observables and their derivatives w.r.t. to arm length variations. In Section IV, we compute the GW responses and sky-averaged sensitivities. In addition, the time-domain waveforms are compared for a quickly chirping GW signal with different TDI observables. Section V presents the parameter inference of this chirping signal and evaluate noise characterizations using simulated data. Finally, a brief conclusion and discussion are given in Section VI. (Throughout this work, we set $G = c = 1$ unless stated otherwise in specific equations.)

II. TIME DELAY INTERFEROMETRY

For the fiducial second-generation TDI Michelson configuration, each observable utilizes four laser interferometric links from two arms. By selecting different initial S/C and sequence, three ordinary observables (X1, Y1, Z1) are defined as follows:

$$X1 : \overrightarrow{121313121} \overleftarrow{131212131}, \quad (1)$$

$$Y1 : \overrightarrow{232121232} \overleftarrow{212323212}, \quad (2)$$

$$Z1 : \overrightarrow{313232313} \overleftarrow{323131323}. \quad (3)$$

In these expressions, the arrows represent the temporal order: " \rightarrow " indicates forward-time direction, and " \leftarrow " means the backward-time direction, which follows the convention in [14], with arm indices modified to correspond to the S/C. For instance, the term $\overrightarrow{121313121}$ in Eq. (1) describes the path S/C1 \rightarrow S/C2 \rightarrow S/C1 \rightarrow S/C3 \rightarrow S/C1 \rightarrow S/C3 \rightarrow S/C1 \rightarrow S/C2 \rightarrow S/C1, as depicted by the blue solid lines in left diagram of Fig. 1. The term $\overleftarrow{131212131}$ in Eq. (1) corresponds to the path represented by the dashed magenta lines, where the temporal order from left to right moves from the latest to the earliest time point. In this work, we focus on the second-generation TDI schemes. For brevity, we refer to the Michelson configuration without explicitly reiterate second-generation.

Following this convention, three ordinary observables of hybrid Relay (U \bar{U} , V \bar{V} , W \bar{W}) are formulated as [1,

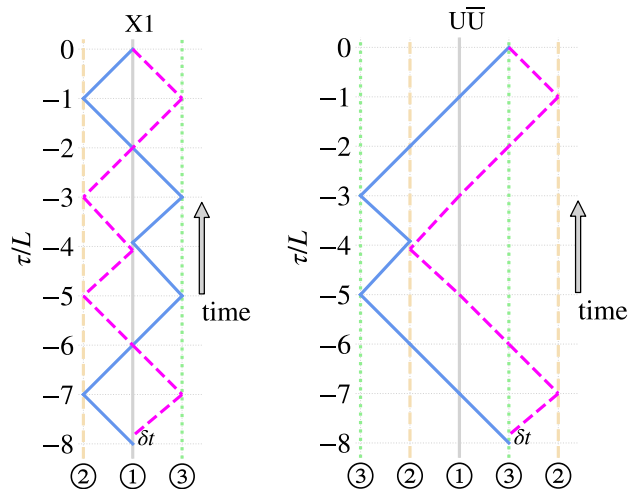


FIG. 1. The geometric diagrams for X1 and U \bar{U} [12, 15]. The vertical lines represent the spacecraft trajectories over time, with \textcircled{i} denoting S/C*i* ($i = 1, 2, 3$). Additional trajectories for S/C2 and S/C3 are plotted to avoid the crossings at noninteger delay time points. The blue solid lines depict the path of one virtual laser beam, while the magenta lines represent the path of another beam. (Diagrams reused from [1].)

12, 15]:

$$U\bar{U} : \overrightarrow{312323213} \overleftarrow{323121323}, \quad (4)$$

$$V\bar{V} : \overrightarrow{123131321} \overleftarrow{131232131}, \quad (5)$$

$$W\bar{W} : \overrightarrow{231212132} \overleftarrow{212313212}. \quad (6)$$

The geometric structure of U \bar{U} is depicted in the right diagram of Fig. 1. As shown by their diagrams, both Michelson and hybrid Relay configurations have a time span of $8L$ ($L \simeq 8.33s$ for LISA). During the TDI process, the maximum delay corresponds to the time interval between the latest and the earliest data points. Since the earliest inter-S/C interferometric links generate data at the receiver S/C, the maximum delay is one arm shorter than the total time span. Consequently, the maximum delays for both Michelson and hybrid Relay are $7L$.

In [12], we developed a series of second-generation TDI observables by combining different first-generation TDI observables. In this work, we focus on identifying TDI observables with a shorter time span. After an initial screening, we identify a second-generation TDI configuration, labeled as PD4L, which is formed by combining the first-generation TDI configurations Beacon (P, Q, R) and Monitor (D, E, F) [4, 5]. Besides the PD4L has the time span as short as $4L$, another key reasons for selecting PD4L is that all its observables, including its null stream, exhibit uniformly minimal null frequencies at m/L , ($m = 1, 2, 3, \dots$). The " $4L$ " in its name distinguishes PD4L from another another TDI scheme labeled PD in [15], which uses different time shifts. The dia-

grams of Beacon-P and Monitor-D are shown in upper panel of Fig. 2 [12]. The first channel of PD4L, denoted as PD4L-1, is expressed as $P(t) + D(t)$, and its geometric representation is depicted in the lower plot of Fig. 2. The paths of three ordinary channels are defined as follows:

$$\text{PD4L-1: } \overrightarrow{123\hat{2}} \overleftarrow{21\hat{2}} \overrightarrow{23\hat{2}\hat{1}} \overleftarrow{1\hat{3}2\hat{3}} \overrightarrow{31\hat{3}} \overleftarrow{\hat{3}2\hat{3}\hat{1}}, \quad (7)$$

$$\text{PD4L-2: } \overrightarrow{231\hat{3}} \overleftarrow{\hat{3}2\hat{3}} \overrightarrow{313\hat{2}} \overleftarrow{\hat{2}1\hat{3}\hat{1}} \overrightarrow{1\hat{2}\hat{1}} \overleftarrow{\hat{1}3\hat{1}\hat{2}}, \quad (8)$$

$$\text{PD4L-3: } \overrightarrow{31\hat{2}\hat{1}} \overleftarrow{\hat{1}3\hat{1}} \overrightarrow{1\hat{2}\hat{1}\hat{3}} \overleftarrow{\hat{3}\hat{2}\hat{1}\hat{2}} \overrightarrow{2\hat{3}\hat{2}} \overleftarrow{\hat{2}\hat{1}\hat{2}\hat{3}}. \quad (9)$$

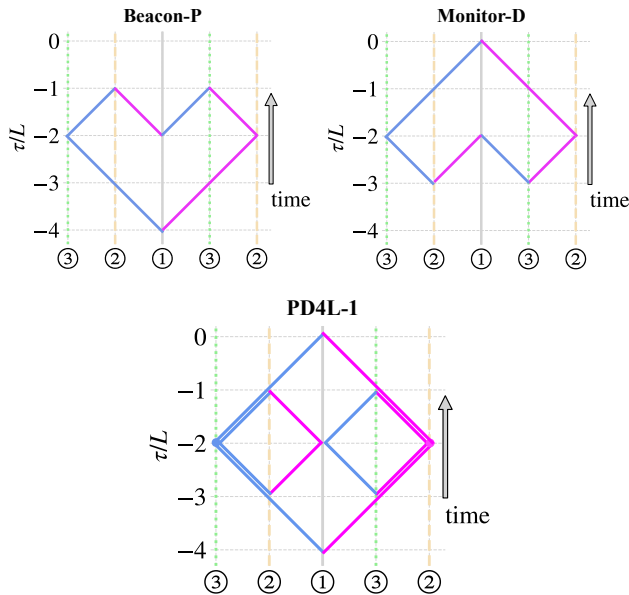


FIG. 2. Geometric diagrams of TDI channels Beacon-P and Monitor-D, and PD4L-1. The Beacon-P and Monitor-D are the first-generation TDI channels shown in upper panel, and the PD4L-1 is the first channel of the second-generation TDI PD4L configuration, formed by combining $P(t) + D(t)$.

For the classical Sagnac and Michelson TDI configurations, three ordinary observables (a, b, c) could be transformed to three (quasi-)orthogonal observables (A, E, T) [16, 17],

$$\begin{bmatrix} A \\ E \\ T \end{bmatrix} = \begin{bmatrix} -\frac{1}{\sqrt{2}} & 0 & \frac{1}{\sqrt{2}} \\ \frac{1}{\sqrt{6}} & -\frac{2}{\sqrt{6}} & \frac{1}{\sqrt{6}} \\ \frac{1}{\sqrt{3}} & \frac{1}{\sqrt{3}} & \frac{1}{\sqrt{3}} \end{bmatrix} \begin{bmatrix} a \\ b \\ c \end{bmatrix}. \quad (10)$$

This transform is applicable when the real part of the cross spectral density (CSD) between two ordinary channels could dominates their imaginary part, as we examined in [2]. Fig. 8 in Appendix A illustrates the real and imaginary components for the PD4L, Michelson and hybrid Relay. The orthogonal transformation is expected to be suitable for PD4L, given that the imaginary parts of its CSDs are two orders of magnitude lower than the real parts. The A and E channels serve as science channels, effectively respond to GWs, while the T channel functions as a null stream, primarily dominated by noises in the low frequency band.

In addition to T channels, which are formed by combining three ordinary channels, specific null streams have been developed. Notable examples include the fully symmetric Sagnac ζ in first-generation TDI [4] and ζ_1 in second-generation TDI [10]. Hartwig and Muratore [13] further developed additional second-generation TDI null streams and analyzed their noise spectra. Among these, C_3^{12} exhibits minimal null frequencies and was employed in [2] to characterize instrumental noise parameters combining with science channels of hybrid Relay. The path of C_3^{12} is expressed as [13, 18]:

$$C_3^{12} : \overrightarrow{1\hat{2}\hat{1}} \overleftarrow{\hat{1}\hat{3}} \overrightarrow{\hat{3}\hat{2}} \overleftarrow{\hat{2}\hat{1}} \overrightarrow{\hat{1}\hat{3}} \overleftarrow{\hat{3}\hat{1}\hat{3}} \overrightarrow{\hat{3}\hat{1}} \overleftarrow{\hat{1}\hat{2}} \overrightarrow{\hat{2}\hat{3}} \overleftarrow{\hat{3}\hat{1}}. \quad (11)$$

Its time span is $2L$, and its geometry is illustrated in Fig. 3 of [2]. To clearly compare the the three TDI configurations and C_3^{12} , a checklist is provided in Table I.

III. NOISE SPECTRA OF TDI

The Michelson TDI observables can effectively suppress laser frequency noises [15, 19–23, and references therein] and mitigate clock noise [24, 25]. The performance of hybrid Relay in suppressing these two types of noises has been evaluated in [1]. The capabilities of PD4L for laser noise suppression and clock noise mitigation are qualified in Appendix B. In this section, we focus on the noise spectra, including acceleration noise and optical metrology system (OMS) noise. Their budgets are setup as [6, 7],

$$\begin{aligned} \sqrt{S_{\text{acc}}} &= 3 \frac{\text{fm/s}^2}{\sqrt{\text{Hz}}} \sqrt{1 + \left(\frac{0.4\text{mHz}}{f}\right)^2} \sqrt{1 + \left(\frac{f}{8\text{mHz}}\right)^4}, \\ \sqrt{S_{\text{oms}}} &= 15 \frac{\text{pm}}{\sqrt{\text{Hz}}} \sqrt{1 + \left(\frac{2\text{mHz}}{f}\right)^4}. \end{aligned} \quad (12)$$

The followings calculations assume identical amplitudes for each type of instrumental noises.

The noise PSDs of the optimal TDI channels from three TDI configurations are presented in the first row of Fig. 3. The results for the A, E, and T channels are arranged from left to right, respectively. To clearly display the values at characteristic frequencies, the x-axis is using $u = fL$, which is dimensionless (where f is frequency and L is the nominal arm length in seconds). A logarithmic scale is utilized for the range $u < 0.1$, while a linear scale is used for higher frequencies. As shown in the first two plots, the science channels for Michelson configuration exhibit null frequency at $u = m/4$, where m is positive integer. In contrast, the alternative science channels, $A_{\text{UU8L}}/E_{\text{UU8L}}$ and $A_{\text{PD4L}}/E_{\text{PD4L}}$, have null frequencies only at $u = m$. The PSDs of the null streams from three TDI configurations, as well as C_3^{12} , are shown in the upper right plot. Among these null channels, T_{PD4L} and C_3^{12} exhibit the fewest null frequencies at $u = m$. The null frequencies in T_{X1} occur at $u =$

TABLE I. Checklist of selected TDI channels. The first column lists the names of the TDI channels. The second column presents the paths of TDI observables, while the third column details links associated with these paths. The fourth column indicates the time span of each channel, defined as the interval from latest (virtual) interferometry time to the initial time of laser emission (where L is the arm length). The fifth column specifies the maximum delay, defined as the time difference between the latest and the earliest data points required to synthesize inter-S/C interferometric measurements. The transform from ordinary channels to the optimal channels is applicable to all three TDI configurations using Eq. (10), with their corresponding optimal/orthogonal observables listed in the sixth column with subscripts. The final column displays the null frequencies in the A/E channel, where m is a positive integer.

channel	TDI path	links	time span	max delay	optimal channels	f_{null} in A/E (m is positive integer)
X1	$\overrightarrow{121313121} \overleftarrow{131212131}$	16	$8L$	$7L$		
Y1	$\overrightarrow{232121232} \overleftarrow{212323212}$	16	$8L$	$7L$	(A_{X1}, E_{X1}, T_{X1})	$m/(4L)$
Z1	$\overrightarrow{313232313} \overleftarrow{323131323}$	16	$8L$	$7L$		
$U\bar{U}$	$\overrightarrow{312323213} \overleftarrow{323121323}$	16	$8L$	$7L$		
$V\bar{V}$	$\overrightarrow{123131321} \overleftarrow{131232131}$	16	$8L$	$7L$	$(A_{U\bar{U}8L}, E_{U\bar{U}8L}, T_{U\bar{U}8L})$	m/L
$W\bar{W}$	$\overrightarrow{231212132} \overleftarrow{212313212}$	16	$8L$	$7L$		
PD4L-1	$\overrightarrow{1232} \overleftarrow{212} \overrightarrow{2321} \overleftarrow{1323} \overrightarrow{313} \overleftarrow{3231}$	16	$4L$	$3L$		
PD4L-2	$\overrightarrow{2313} \overleftarrow{323} \overrightarrow{3132} \overleftarrow{2131} \overrightarrow{121} \overleftarrow{1312}$	16	$4L$	$3L$	$(A_{PD4L}, E_{PD4L}, T_{PD4L})$	m/L
PD4L-3	$\overrightarrow{3121} \overleftarrow{131} \overrightarrow{1213} \overleftarrow{3212} \overrightarrow{232} \overleftarrow{2123}$	16	$4L$	$3L$		
C_3^{12}	$\overrightarrow{121} \overleftarrow{13} \overrightarrow{32} \overleftarrow{21} \overrightarrow{13} \overleftarrow{313} \overrightarrow{31} \overleftarrow{12} \overrightarrow{23} \overleftarrow{31}$	12	$2L$	L		m/L

$m/4$, and more null frequencies appear in $T_{U\bar{U}8L}$. The calculations are implemented by using a random time point from a numerical orbit [26] [27], and the instantaneous arm length are $[L_{12}, L_{21}, L_{13}, L_{31}, L_{23}, L_{32}] \simeq [8.296, 8.297, 8.275, 8.277, 8.313, 8.313]$ s.

The noise spectra are functions of instrumental noises (acceleration noise and OMS noise) and arm lengths between the S/C. Therefore, although the instrumental noises are assumed to be stationary, the noise PSDs will change with orbital evolution due to variations in the arm lengths resulting from orbital dynamics. To evaluate the stabilities of noise spectra, their derivatives w.r.t. three arm lengths are calculated. The second to fourth rows in Fig. 3 show the derivatives w.r.t L_{12} , L_{13} , and L_{23} , respectively. During the calculation, the deviations in L_{ij} and L_{ji} are treated as equal, and $\frac{\partial \ln S_n}{\partial L_{ij}}$ includes the effects of deviations in both L_{ij} and L_{ji} , even though they could be slightly different in a realistic case. Generally, the curves exhibit sharp peaks around their null frequencies because the noise spectra at these frequencies are significant low and highly sensitive to changes in the arm lengths. The downward spikes are primarily caused by sign reversals during the process of taking the absolute values.

For two science channels, A and E, their derivatives are shown in the first two columns. The spectra of X1 and $U\bar{U}8L$ (with $8L$ time span) are more robust than PD4L in the lower frequency band ($u < 0.1$). Their derivatives, $\frac{\partial \ln S_n}{\partial L_{ij}}$, are consistently below 0.2 for all three arms as indicated by the dashed curves. In contrast, the PD4L shows notable differences for varying arm length changes

in this band. One reason for this is that a shorter time span results in lower noise PSDs in low frequency range in science channels, as shown in the first row of Fig. 3. These deviations are relatively pronounced in its TDI channels compared to those with higher PSDs. In the high frequency range ($u > 0.1$), the stability of TDI channels varies significantly for each case. Michelson observables are less favored due to their unstable spectra, which are strongly affected by its null frequencies. The science channels of hybrid Relay are more stable, with derivatives amplitudes ranging in $\sim [0.1, 1]$, except around the null frequencies. The stability of science channels for PD4L depends on the changes in different arms and the frequency band. The fluctuations around the null frequencies could be higher than those of the hybrid Relay, but it may also be lower than hybrid Relay in the middle frequencies between two null frequencies. The noise spectrum of E_{PD4L} remains highly stable when the L_{12} and L_{23} change.

The evaluations of the null streams are shown in the right column of Fig. 3. As indicated by the dashed blue curves, T_{X1} is significantly unstable, which could potentially undermine the accuracy of data analysis [1, 2, 28]. Its derivatives exhibit large variations with respect to different arms, especially in the lower frequency band. For the other null channels, the derivatives w.r.t. the three arms are nearly identical. Among these null streams, T_{PD4L} is the most stable across the target frequency range (except at null frequencies), as shown by the sold green curves. $T_{U\bar{U}8L}$ is stable for $u < 0.1$, but becomes unstable at higher frequencies. C_3^{12} is generally stable across frequency band as shown by the red curve, but its

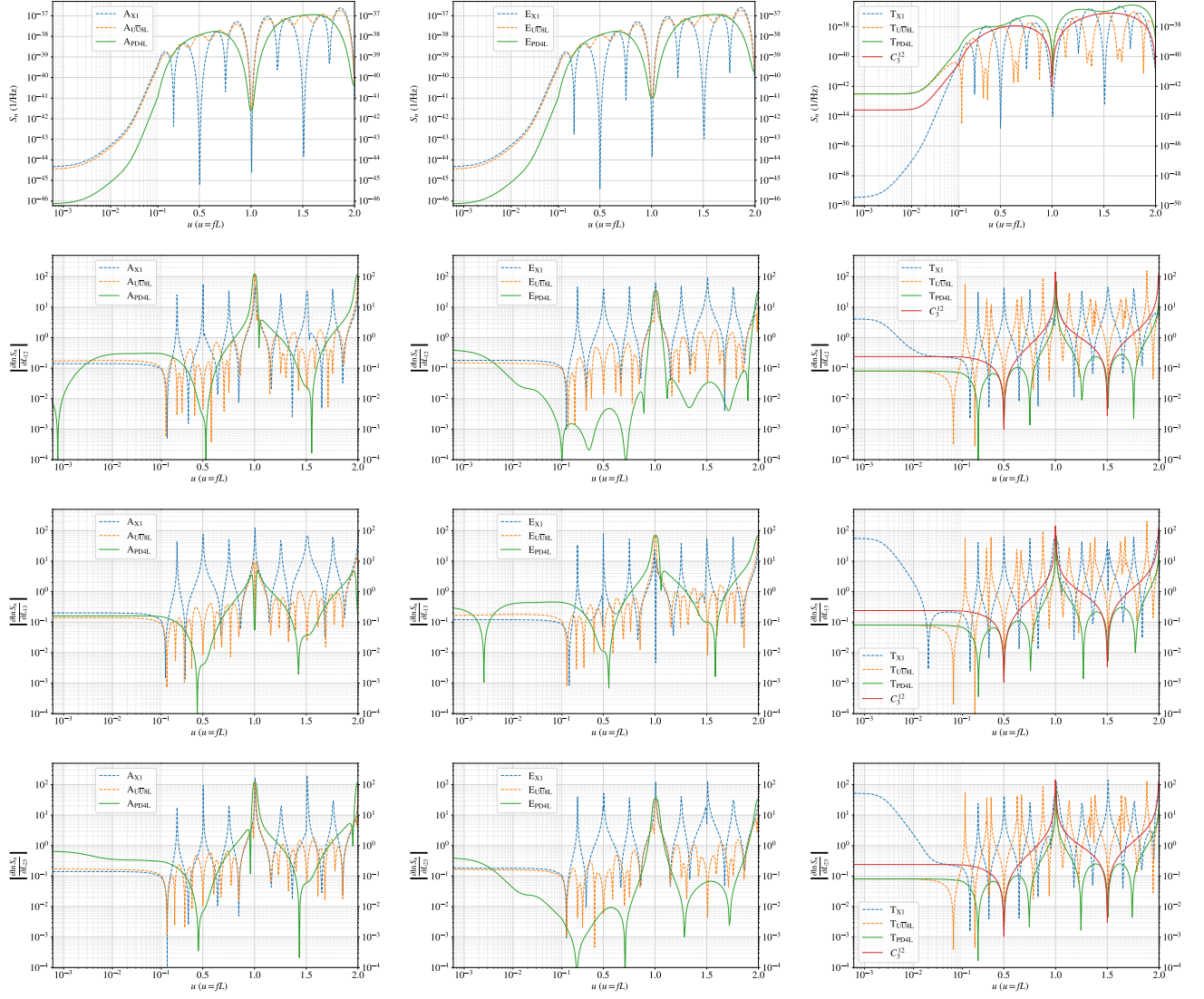


FIG. 3. The noise PSDs (first row) and their derivatives w.r.t the arm lengths (second to fourth rows) for optimal observables of selected TDI configurations. The results for the A, E, and T channels are arranged from left to right columns. The specific null stream, C_3^{12} , is plotted together with other three T channels for comparison. As their noise PSDs shown in the first row, two science channels, A and E, are identical for each TDI configuration. The Michelson configuration has null frequency at $u = m/4$ ($m = 1, 2, 3, \dots$), while the science channels of hybrid Relay and PD4L, as well as T_{PD4L} and C_3^{12} exhibit null frequencies at $u = m$. The second to fourth rows show the derivatives w.r.t the L_{12} , L_{13} , and L_{23} , respectively. Although the PSDs of A and E are identical, they are affected differently by the changes in arm lengths. The most significant divergences in the derivatives appear around the null frequencies because of the very low PSDs. Therefore, the Michelson (dashed blue curves) is the most unstable configuration at higher frequencies due a large number of null frequencies. The science channels of hybrid Relay (dashed orange curves) are more stable benefiting from fewer null frequencies. The channels of PD4L (solid green curves) show varied stability depending on the changes in arm lengths and frequency band. At lower frequencies, the science channels of PD4L are relatively unstable compared to other two configurations. The fluctuations around null frequencies could be higher than those of hybrid Relay, but it may also be lower than hybrid Relay in the middle frequencies between two null frequencies. The noise spectrum of E_{PD4L} remains highly stable when the L_{12} and L_{23} change. Its T channel, T_{PD4L} , is the most robust one among the selected null streams as shown in left column. The C_3^{12} is generally stable across the frequency band, but its level is worse than that of T_{PD4L} .

level of stability is lower than that of T_{PD4L} .

IV. RESPONDED GW BY TDI

The sky-averaged response of a TDI channel to GW is calculated by using

$$\mathcal{R}_{\text{TDI}}(f) = \frac{1}{4\pi} \int_0^{2\pi} \int_{-\pi/2}^{\pi/2} |F_{\text{TDI}}^{\text{GW}}(f)|^2 \cos \beta d\beta d\lambda, \quad (13)$$

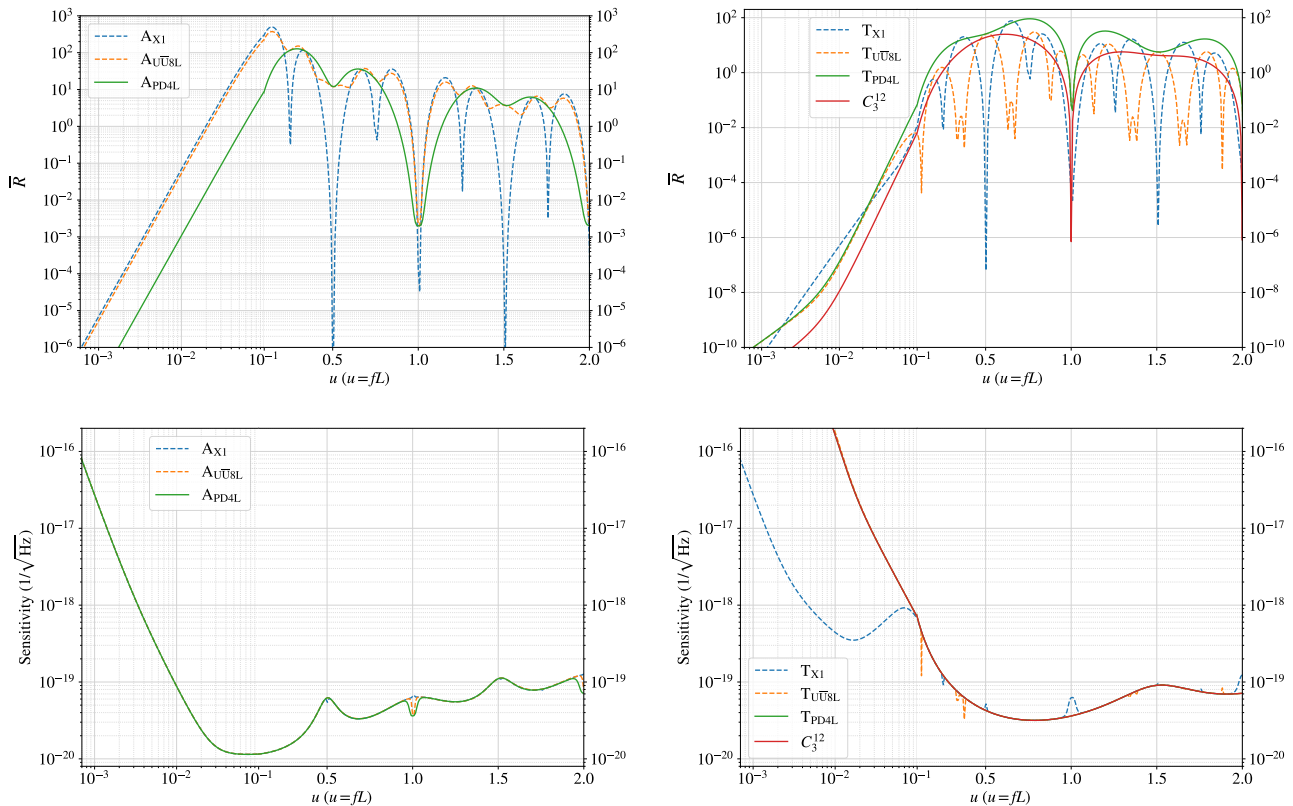


FIG. 4. The average GW response (upper row) and sensitivities (lower row) of selected TDI channels. The left column shows results for science A channels, and the right column depicts the null streams. The spikes in sensitivities are caused by numerical error at their null frequencies. In the lower right plot, the curves of T_{UU8L} , T_{PD4L} and C_3^{12} are overlapping.

where (λ, β) are the ecliptic longitude and latitude. The responses are normalized by u^2 , $\bar{\mathcal{R}} = \mathcal{R}_{\text{TDI}}(f)/u^2$, and are shown in the upper panel of Fig. 4. The corresponding average sensitivities are calculated by using $\sqrt{\frac{S_{n, \text{TDI}}}{\mathcal{R}_{\text{TDI}}}}$ and presented in the lower panel. The science and null channels are shown in the left and right columns, respectively. Since the average responses and sensitivities of the A and E channels are identical, only A channels are presented. As shown in the upper left plot, the average responses of A_{UU8L} and A_{PD4L} are smoother than the Michelson in the higher frequency range ($u > 0.1$), benefiting from fewer null frequencies. At lower frequencies for $u < 0.1$, the response of A_{PD4L} is approximately two orders of magnitude lower than that of A_{X1} or A_{UU8L} . This indicates greater suppression of GW signals during the TDI process of PD4L. This reduction is due to the shortening of the time span from $8L$ to $4L$, which leads to greater signal cancellation in the long-wavelength regime. However, as shown in the lower left plot, the average sensitivities of three science channels are essentially identical. This is because the lower GW response in PD4L is counterbalanced by the lower noise PSD, as compared in the first plot of Fig. 3, resulting in an equal average sensitivity as other two TDI configurations. The trade-off for using PD4L is that its TDI process may require a

higher precision interpolation algorithm compared to the Michelson or hybrid Relay configuration [29, 30].

The responses and sensitivities of four noise streams are shown in the right column of Fig. 4. As seen in the upper plot, the responses of T_{PD4L} and C_3^{12} are the smoothest, represented by the solid green and red curves. And the amplitude of T_{PD4L} is higher than that of C_3^{12} across the full frequency band. In contrast, the responses of T_{X1} and T_{UU8L} , due to their higher number of null frequencies, exhibit significant fluctuations in the high frequency band. The lower right plot of Fig. 4 presents the average sensitivities of four channels. T_{X1} appears to be more sensitive at low frequencies for $u < 0.1$. However, this improvement is correlated with its E channel as analyzed in [2, 31]. The other three null channels exhibit nearly identical sensitivities, as indicated by their overlapping curves.

TDI operations are applied for a rapidly chirping signal generated by a MBBH with masses $m_1 = 3 \times 10^4 M_\odot$ and $m_2 = 1 \times 10^4 M_\odot$ at redshift $z = 0.2$. The goal is to compare the responses of different TDI observables to a high-frequency signal. The merging signal is shown in the first row of Fig. 5. The blue and orange frames indicate the time span of TDI operation for $8L$ (Michelson or hybrid Relay) or $4L$ (PD4L), respectively. The three pairs

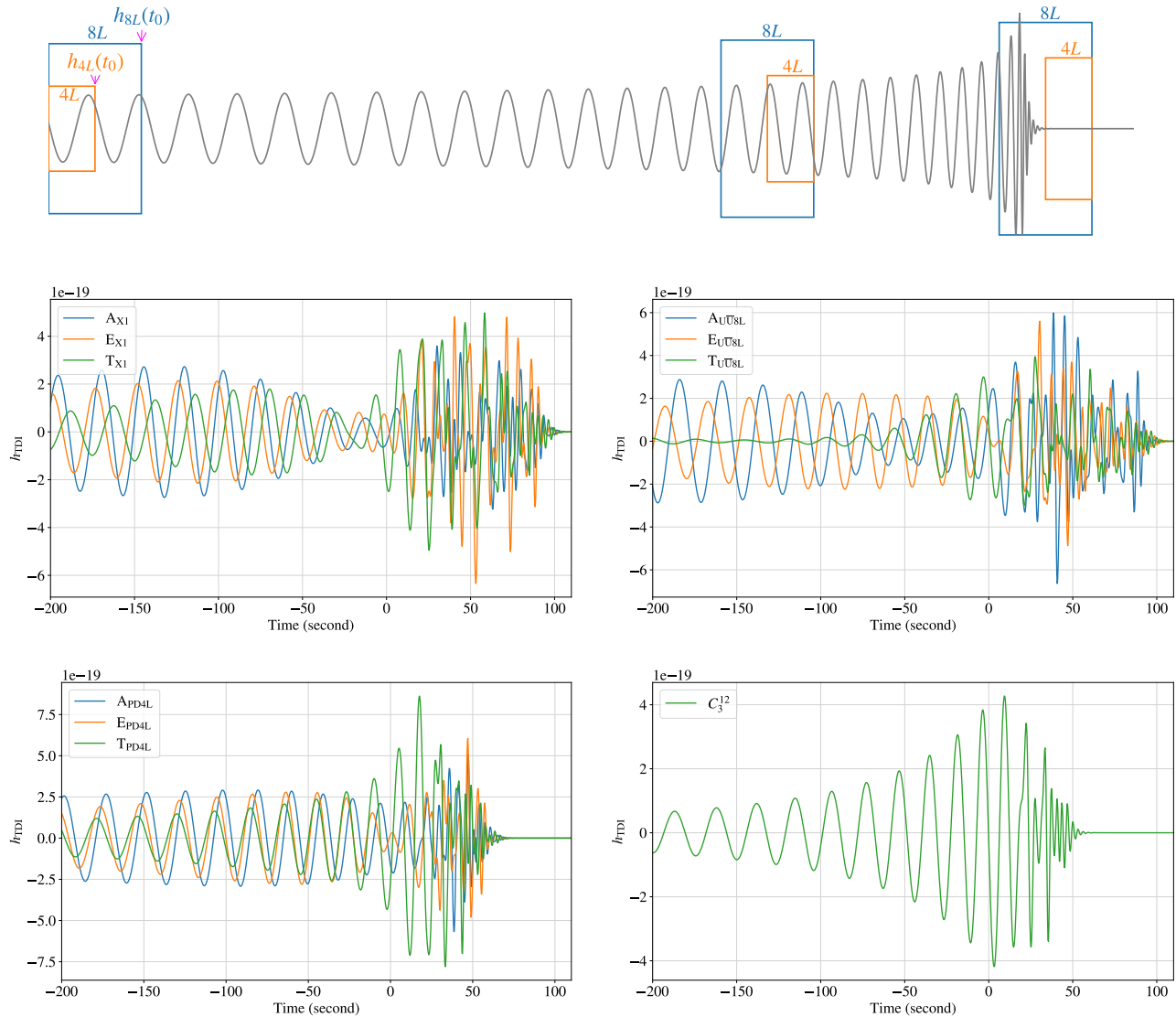


FIG. 5. A merging GW signal from a MBBH ($m_1 = 3 \times 10^4 M_\odot$, $m_2 = 1 \times 10^4 M_\odot$ at $z = 0.2$) and the corresponding waveforms in TDI channels. The first row shows the original waveform, with the blue and orange frames illustrate time span of TDI operation for $8L$ (Michelson and hybrid Relay) and $4L$ (PD4L) configurations. The three pairs of frames, from left to right, illustrate: 1) margin effects at the data boundary, 2) frequency aliasing at high frequency band, and 3) tails effects at the end of the signal. (Note that realistic TDI involves responded GW across multiple inter-S/C links.) The middle and lower rows display the responded waveforms in selected TDI channels. The merger signal arriving at the solar-system barycenter is set to be $t = 0$, and the signal later reaches the detector in this simulation. The middle left plot depicts the waveforms in the Michelson optimal channels (A_{X1} , E_{X1} , T_{X1}), and the middle right plot displays waveforms from hybrid Relay ($A_{U\bar{U}8L}$, $E_{U\bar{U}8L}$, $T_{U\bar{U}8L}$). The lower left plot illustrates the waveforms for PD4L configuration, and the waveform in null stream C_3^{12} is shown in the lower right panel. Compared to these waveforms, TDI observables with shorter time spans yield smoother waveforms with shorter tails at the end of signal.

of frames from left to right illustrate three key aspects:

- **Data Margin:** TDI channels with shorter span generate data earlier and reduce margin effects at the data boundary. For example, in Michelson TDI, the first data point is generated at $\sim 8L$ after the S/C initially emits the laser signal, whereas PD4L advances this to $\sim 4L$.
- **Frequency Aliasing,** longer-span TDI configurations will more easily cross the periods of signal and experience more significant frequency aliasing..
- **Tail Effects,** more compact TDI configurations will more quickly pass through the end of signal and result in shorter tails at the end.

We emphasize that realistic TDI is more complex, involv-

ing GW responses across multiple inter-S/C links rather than the simplified waveform presented here. The responded waveforms in the orthogonal channels of Michelson, hybrid Relay and PD4L, as well as the null stream C_3^{12} , are presented in the second and third rows of Fig. 5. In this simulation, the merge time arriving at solar-system barycenter is set to be $t = 0$. Due to the source direction and detector location setups, the merger appears later in the TDI channels.

Comparing the waveforms in these TDI channels with different time span, the waveforms of Michelson observables exhibit irregular amplitudes and phases variations around the merging due to aliasing and modulations near null frequencies. In right plot of second row in Fig. 5, the waveform amplitudes of hybrid Relay experience less modulation compared to Michelson, benefiting from fewer null frequencies. However, the phases remain arrhythmic due to mixed phase contributions across different periods. In contrast, the waveforms in PD4L observables (lower left plot) are noticeably smoother since aliasing effects are mitigated with shorter range. Additionally, PD4L waveforms have shorter tails at the end, as this configuration is $4L$ more compact than Michelson and hybrid Relay. With minimal null frequencies in all three orthogonal channels, the PD4L waveforms maintain better phase coherence. In the lower right plot, the TDI C_3^{12} effectively captures high frequency signals. Benefiting from its minimal null frequencies and shortest $2L$ time span, the waveform in C_3^{12} exhibits the smoothest phase evolution and the shortest tail compared to other three TDI configurations.

These comparisons suggest that TDI configurations with shorter time spans are better suited for processing the data, particular in the high frequency band. The resulting smoother waveforms facilitate signal modeling in the frequency-domain. In the next section, we perform parameter inference for this chirp signal and compare the performance of different TDI configurations.

V. PARAMETER INFERENCE WITH SIMULATED DATA

In this section, two types of inferences are conducted: 1) inferring the parameters of the chirp signal described in Section IV to compare the capabilities of TDI configurations in analyzing high-frequency signals, 2) estimating the amplitudes of noises components using pure noise data to assess the performance in noise characterization. The parameter inferences are performed using simulated data with different TDI configurations. Time-domain noise data for each ordinary TDI observable are generated using SATDI [32], incorporating acceleration noise and OMS noise under assumptions of Gaussian and stationary properties. For each TDI configuration with three ordinary data streams, the corresponding (quasi-)orthogonal data are obtained by applying transformation of Eq. (10).

For the first type of inference, the GW signal is injected into the simulated data. The signal corresponds to a spinless MBBH with component masses $m_1 = 3 \times 10^4 M_\odot$ and $m_2 = 10^4 M_\odot$ in the source frame at redshift $z = 0.2$. This corresponds to a luminosity distance of $d_L = 1012.3$ Mpc [33, 34]. The signal lasts for 3 hours before its coalescence, with the frequency evolving from 0.01 Hz to 0.3 Hz in the detector frame. This short duration and high-frequency range are deliberately chosen to assess the TDI performances for high-frequency signals. The source direction is set with ecliptic longitude $\lambda = 4.6032$ rad and ecliptic latitude $\beta = \pi/10$ rad, and the polarization angle is chosen as $\psi = 0.55$ rad. The inclination angle between the binaries' rotation axis and the line-of-sight is set to $\iota = \pi/3$. The merger time, $t_c = 0$, corresponds to the moment the merger reaches the solar-system barycenter, with a reference phase ϕ_c . The time-domain waveform is generated using the SEOBNRv4HM model [35]. During the inference, we infer the redshifted chirp mass $\mathcal{M}_c = (m_1 m_2)^{3/5} / (m_1 + m_2)^{1/5}$ and mass ratio $q = m_2 / m_1$ instead of inferring individual component masses. And we also estimate the time shift Δt_c relative to the merger time. The frequency-domain waveform is generated from a reduced-order version of the SEOBNRv4HM [36]. Nine parameters are inferred [$\mathcal{M}_c, q, d_L, \iota, \lambda, \beta, \psi, \Delta t_c, \phi_c$].

For noise characterization, we infer 12 parameters describing the amplitudes of acceleration noises and OMS noises with PD4L configuration. As specified in Eqs. (12), six parameters for acceleration noise amplitudes are set to be $A_{accij} = 3$, where ij represents the pair of S/C i facing to S/C j . Another six parameters for amplitudes of OMS noise are set to be $A_{omsij} = 15$. And their square values are estimated during the characterization. The priors for the acceleration noise amplitude, A_{acc}^2 , are uniformly distributed within a range of $[0, 40]$, and the priors for the OMS noises amplitude, A_{oms}^2 , are set in the range $[50, 300]$. The inference is performed in the frequency-domain with a low-frequency cutoff at 0.03 mHz and a high-frequency cutoff at 0.1 Hz.

The parameter estimation is performed using the Bayesian algorithm. The likelihood function is given by [37, 38]:

$$\ln \mathcal{L}(d|\vec{\theta}) = \sum_{f_i} \left[-\frac{1}{2} \tilde{\mathbf{n}}^T \mathbf{C}^{-1} \tilde{\mathbf{n}}^* - \ln(\det 2\pi \mathbf{C}) \right]. \quad (14)$$

where $\tilde{\mathbf{n}}$ is the frequency-domain noise data vector. In the case for analyzing MBBH, it represents the data after the chirp signal has been subtracted. The matrix \mathbf{C} is the noises correlation matrix for the three orthogonal channels:

$$\mathbf{C} = \frac{T_{\text{obs}}}{4} \begin{bmatrix} S_{AA} & S_{AE} & S_{AT} \\ S_{EA} & S_{EE} & S_{ET} \\ S_{TA} & S_{TE} & S_{TT} \end{bmatrix}, \quad (15)$$

where T_{obs} is the data duration. The inference is performed using the nested sampler MultiNest [39, 40].

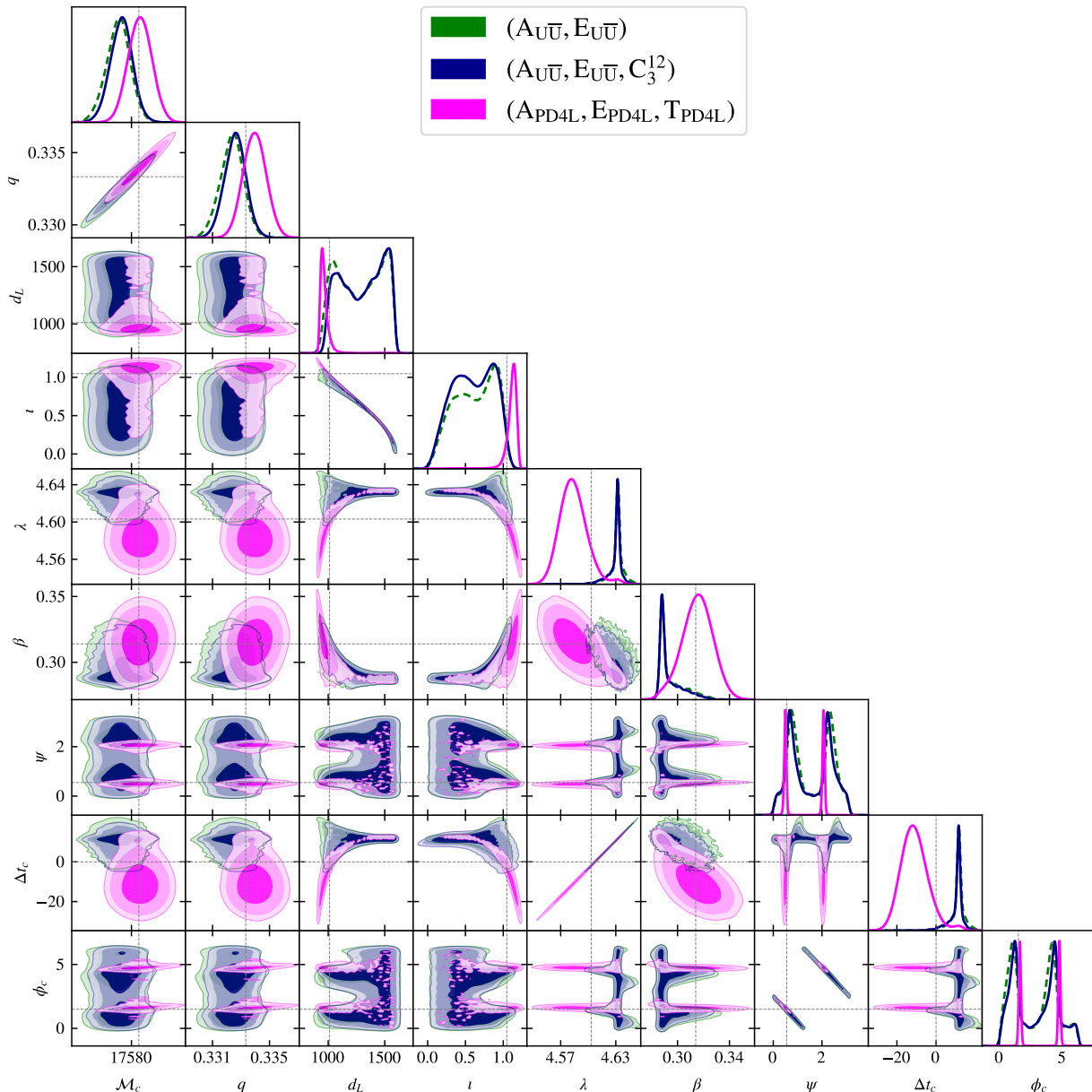


FIG. 6. Inferred parameter distributions from three TDI combinations. The gradients represent the 1σ , 2σ , and 3σ confidence regions from darker to lighter. The grey dashed lines indicate the simulated parameter values. The green regions show the distribution obtained from two science channels of hybrid Relay ($A_{U\bar{U}8L}$, $E_{U\bar{U}8L}$), and the blue areas indicate the distribution with the additional C_3^{12} channel ($A_{U\bar{U}8L}$, $E_{U\bar{U}8L}$, C_3^{12}). The magenta contours display the results from three optimal channels of PD4L (A_{PD4L} , E_{PD4L} , T_{PD4L}).

Three combinations of TDI observables are used to estimate the parameters of the MBBH source: 1) employing two science channels from hybrid Relay ($A_{U\bar{U}8L}$, $E_{U\bar{U}8L}$), 2) combining two science observables of hybrid Relay and null stream C_3^{12} ($A_{U\bar{U}8L}$, $E_{U\bar{U}8L}$, C_3^{12}), as we proposed for optimal noise characterization in [2], and 3) utilizing three orthogonal observables from PD4L configuration (A_{PD4L} , E_{PD4L} , T_{PD4L}). The parameter distributions inferred from these three cases are shown in Fig.

6. The distributions obtained from ($A_{U\bar{U}8L}$, $E_{U\bar{U}8L}$) and ($A_{U\bar{U}8L}$, $E_{U\bar{U}8L}$, C_3^{12}) are represented by the green and blue regions, respectively. Those two results are largely consistent, with only minor differences for the distance and inclination parameters. However, both distributions barely include the true values of extrinsic parameters in the 3σ regions. The parameter distributions inferred from (A_{PD4L} , E_{PD4L} , T_{PD4L}) are represented by magenta contours, and all true values are within the 2σ re-

gions. Additionally, the marginalized distributions from the PD4L observables are closer to Gaussian shapes compared to the other two combinations, suggesting that the signal is better modeled, even though the same algorithm is used.

The results for noise characterization are shown in Fig. 7. Data from three durations are utilized using the optimal channels of PD4L (A_{PD4L} , E_{PD4L} , T_{PD4L}). The blue, magenta, and green regions represent the parameters distributions for the 120-day, 150-day and 180-day durations, respectively. Since acceleration noises from paired test masses on an interferometric link are correlated, their quadratic sums, $A_{\text{acc}ij} + A_{\text{acc}ji}$, are shown in the left plot. As expected, the uncertainties decrease as the duration increases. The values of acceleration noise parameters are effectively captured within the 2σ regions for all three durations. The distributions of six OMS noise parameters, $A_{\text{OMS}ij}^2$, are shown in the right plot. For the 120-day duration, the simulated values are well encompassed within the 3σ regions. However, for the 150-day and 180-day durations, the true values are not fully included in 3σ regions. This indicates that the noise characterization capability of PD4L combination is slightly weaker than the combination ($A_{\text{U}\bar{\text{U}}8L}$, $E_{\text{U}\bar{\text{U}}8L}$, C_3^{12}), which accurately determined the parameters with a 180-day data [2]. This difference should be due to the noise spectra of (A_{PD4L} , E_{PD4L}) being less robust compared to those of ($A_{\text{U}\bar{\text{U}}8L}$, $E_{\text{U}\bar{\text{U}}8L}$), as shown in Fig. 3.

The current simulation and analysis do not account for data gap. The LISA mission is expected to have a duty cycle of $>82\%$ [7]. If the data is divided into chunks shorter than ~ 4 months due to gaps, the PD4L should still meet the requirement for accurate noise characterization. Giving its superior performance in processing GW signals in the higher frequency band, the PD4L configuration could be a viable alternative TDI configuration.

VI. CONCLUSION AND DISCUSSION

In this work, we introduce a second-generation TDI, PD4L, which features minimal null frequencies and operates over a shorter time span of $4L$ – half that of the fiducial Michelson or hybrid Relay with $8L$. This compact design brings three primary advantages: 1) the data margin required for TDI operation is reduced by $4L$ compared to Michelson or hybrid Relay; 2) aliasing in the high frequency band is mitigated; and 3) the tail at the end of a signal is shortened. These benefits make the PD4L configuration particularly advantageous for high-frequency signal analysis in the frequency domain. However, two disadvantages are also identified: 1) both GW signal and noise suppression are more pronounced in the low frequency band, which may demand higher precision during interpolation to reconstruct data values at any time delay; 2) the noise spectra in two science channels are less stable than those of hybrid Relay, which constrains the duration over which noise characterization reliable.

To qualify the performance of PD4L, we simulated a rapidly chirping signal and compared the response across different TDI observables. Subsequent parameter inferences results demonstrate that PD4L outperforms the hybrid Relay in terms of accuracy. Given that the hybrid Relay already surpasses the Michelson configuration [1, 2], we deduce the PD4L provides the best capability among these three TDI configurations for analyzing high frequency signals, specifically in the band $u = fL > 0.1$. On the other hand, despite the relatively lower noise stability of PD4L’s science channels than that of hybrid Relay, and its somewhat limited noise characterization capability, its T channel, T_{PD4L} , emerges as the most stable null stream identified in our investigations to date.

While our current GW signal inferences are performed in the frequency domain, we acknowledge that our current frequency-domain model may not be optimally match signal though the Fourier transform of a finite time-domain data. Tail effects and aliasing introduced by TDI operations could not be well accounted for, potentially leads to biases into parameter estimation. A more compact TDI configuration mitigate, rather than completely resolves, these effects compared to longer-span TDI schemes. In a recently work, García-Quirós *et al.* [41] demonstrated a GPU-accelerated parameter inference utilizing time domain responses, which could help address the shortages in the frequency-domain models.

In Wang [12], we developed a variety of TDI configurations by combining the first-generation observables, identifying some of those with minimized null frequencies across time spans of $4L$, $6L$, and $8L$. We selected the hybrid Relay and PD4L as representative configurations for the $8L$ and $4L$ spans, respectively. Notably, PD4L’s null stream exhibits the same minimal frequencies as its science channels, a unique feature among the TDI configurations we examined. In a forthcoming work [42], we will systematically analyze the differences and correlations between these configurations.

ACKNOWLEDGMENTS

G.W. was supported by the National Key R&D Program of China under Grant No. 2021YFC2201903, and NSFC No. 12003059. This work made use of the High Performance Computing Resource in the Core Facility for Advanced Research Computing at Shanghai Astronomical Observatory. This work are performed by using the python packages `numpy` [43], `scipy` [44], `pandas` [45], `MultiNest` [39] and `PyMultiNest` [40], and the plots are make by utilizing `matplotlib` [46], `GetDist` [47].

Appendix A: Orthogonalizatable of TDI configurations

The covariance matrix of noises from three ordinary channels (a, b, c) of a TDI configuration can be expressed

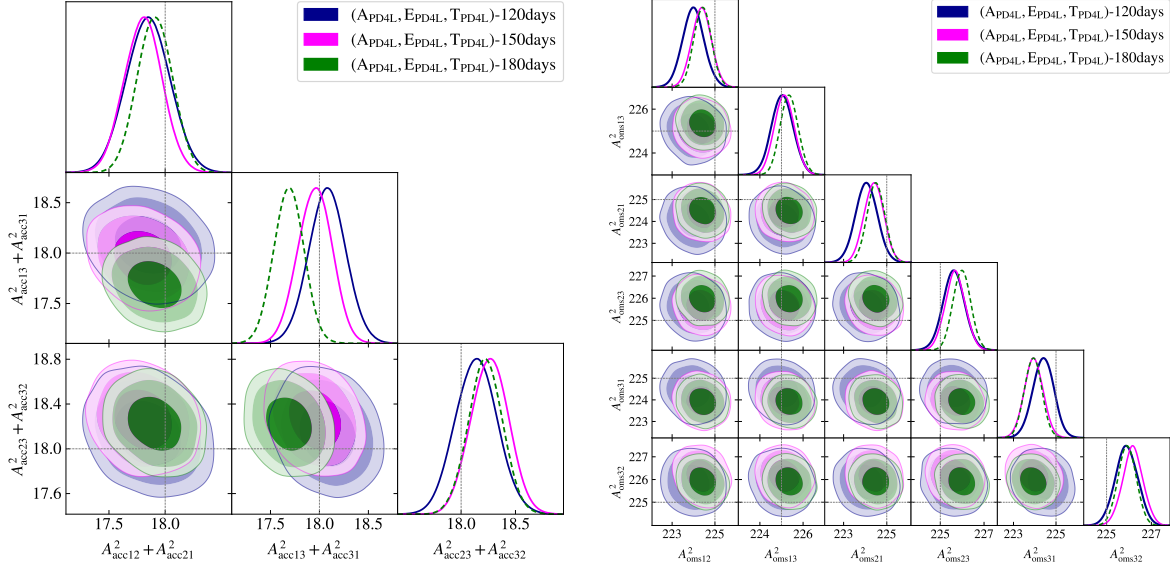


FIG. 7. The inferred parameter distributions from 120-day, 150-day, and 180-day data streams (A_{PD4L} , E_{PD4L} , T_{PD4L}) based on a dynamic unequal-arm constellation with a low-frequency cutoff at 0.03 mHz and a high-frequency cutoff at 0.1 Hz. The gradients show the 1σ , 2σ , and 3σ regions from darker to lighter. The grey dashed lines indicate the simulated values. The left plot shows the quadratic sums of acceleration noise amplitudes, and the right plot presents the squared amplitudes of OMS noise.

as

$$\begin{bmatrix} S_a & S_{ab} & S_{ac} \\ S_{ba} & S_b & S_{bc} \\ S_{ca} & S_{cb} & S_c \end{bmatrix} \simeq \begin{bmatrix} S_a & S_{ab} & S_{ab} \\ S_{ab} & S_a & S_{ab} \\ S_{ab} & S_{ab} & S_a \end{bmatrix}, \quad (A1)$$

where S_a represents PSD of data stream a , and S_{ab} denotes cross spectral density (CSD) of data stream a and b . In a realistic scenario, the CSDs of S_{ab} and S_{ba} are complex conjugates. However, the orthogonal transform remains valid if the real part of the CSD dominates the imaginary part. Fig. 8 illustrates the CSDs of first two ordinary channels in the Michelson, hybrid Relay, and PD4L configurations. The real components are shown by the solid curves, and the corresponding imaginary parts are shown by the dashed curves with the same colors. As observed, the real components are orders of magnitude higher than their imaginary components in all three CSDs. Therefore, the approximation of the (quasi-)orthogonal transformation using (10) is applicable for these three TDI configurations.

Appendix B: laser noise and clock noise suppression

As a second-generation TDI configuration, it is essential for PD4L to sufficiently suppress the laser frequency noise. Assuming a laser stability of $30 \text{ Hz}/\sqrt{\text{Hz}}$, this corresponds to a noise PSD of $1 \times 10^{-26} \text{ /Hz}$. The ranging error between S/C is modeled with a PSD of $10^{-15} \frac{\text{Hz}}{f} \text{ s}/\sqrt{\text{Hz}}$ and an additional bias of 3 ns (0.9 m) [23, 48]. Based on these noise assumptions, the residual

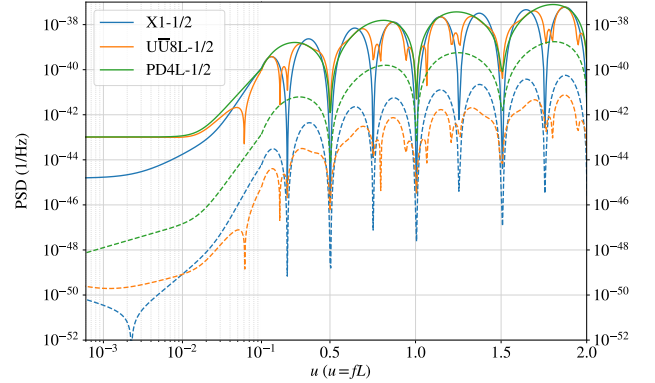


FIG. 8. The real (solid curves) and imaginary (dashed curves) components of CSDs between two ordinary TDI channels for selected configurations. Each pair of solid and dashed curves represents the respective real and imaginary parts of a CSD. The real components are several orders of magnitude higher than the imaginary parts, ensuring the validity of the transformation from ordinary channels to (quasi-)orthogonal channels.

laser noise in PD4L-1 is evaluated and presented by the orange curves in the upper panel of Fig. 9. For comparison, secondary noises sources, including acceleration noise and OMS noise, are also plotted (blue curves). As we can read from the plot, the residual laser noise in PD4L is orders of magnitude lower than the secondary noises.

The clock noise in PD4L-1 is assessed assuming a clock noise of $4 \times 10^{-27}/f$ in fractional frequency deviations. As shown in lower panel of Fig. 9, clock noise in TDI observable exceeds secondary noise at lower frequencies. However, after applying the subtraction method proposed in [25], the residual clock noise (green curve) is well below secondary noise level. Therefore, the PD4L TDI configuration meet the fundamental requirement for effective noise suppressions.

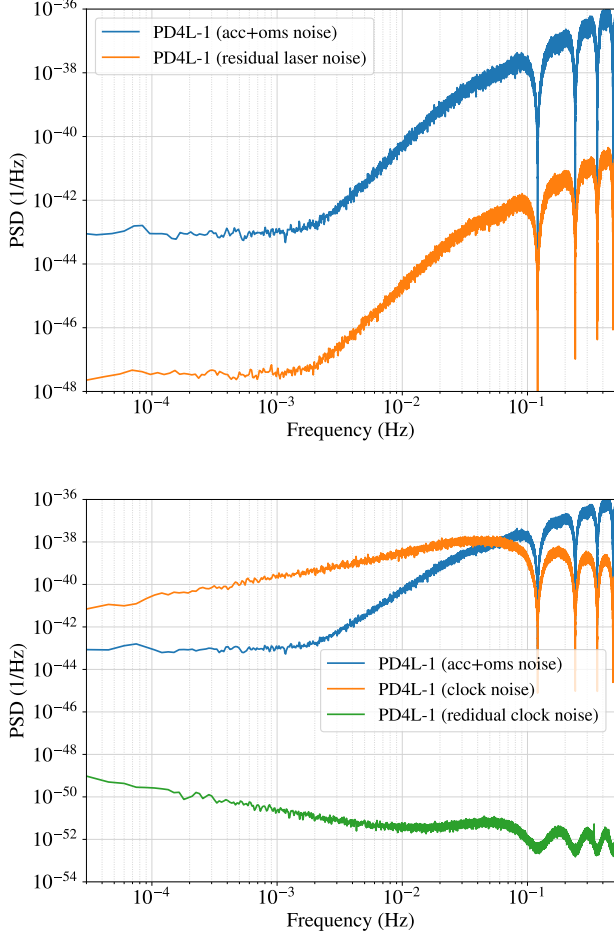


FIG. 9. The spectra of residual laser noise (upper panel) and clock noise (lower panel) in the PD4L-1 channel. The secondary noises, including acceleration noise and OMS noise, are shown in blue for comparison. In the upper plot, residual laser noise arising from ranging errors and orbital dynamics is several orders of magnitude lower than the secondary noise. In the lower plot, the clock jitter noise is shown by orange curve, while the green curve represents the residual clock noise after applying the subtraction method from [25].

[1] G. Wang, Time delay interferometry with minimal null frequencies, Phys. Rev. D **110**, 042005 (2024), (Paper I),

arXiv:2403.01490 [gr-qc].
 [2] G. Wang, Enhancing noise characterization with robust

- time delay interferometry combination, *Phys. Rev. D* **110**, 064085 (2024), (Paper II), arXiv:2406.11305 [gr-qc].
- [3] W.-T. Ni, J.-T. Shy, S.-M. Tseng, X. Xu, H.-C. Yeh, W.-Y. Hsu, W.-L. Liu, S.-D. Tzeng, P. Fridelance, E. Samain, D. Lee, Z.-Y. Su, and A.-M. Wu, Progress in mission concept study and laboratory development for the ASTROD (Astrodynamical Space Test of Relativity using Optical Devices), in *Small Spacecraft, Space Environments, and Instrumentation Technologies*, Society of Photo-Optical Instrumentation Engineers (SPIE) Conference Series, Vol. 3116, edited by F. A. Allahdadi, E. K. Casani, and T. D. Maclay (1997) pp. 105–116.
- [4] J. W. Armstrong, F. B. Estabrook, and M. Tinto, Time-Delay Interferometry for Space-based Gravitational Wave Searches, *Astrophys. J.* **527**, 814 (1999).
- [5] F. B. Estabrook, M. Tinto, and J. W. Armstrong, Time-delay analysis of LISA gravitational wave data: Elimination of spacecraft motion effects, *Phys. Rev. D* **62**, 042002 (2000).
- [6] P. Amaro-Seoane, H. Audley, S. Babak, and et al (LISA Team), Laser Interferometer Space Antenna, arXiv e-prints, arXiv:1702.00786 (2017).
- [7] M. Colpi *et al.*, LISA Definition Study Report, (2024), arXiv:2402.07571 [astro-ph.CO].
- [8] W.-R. Hu and Y.-L. Wu, The Taiji Program in Space for gravitational wave physics and the nature of gravity, *Natl. Sci. Rev.* **4**, 685 (2017).
- [9] J. Luo *et al.* (TianQin), TianQin: a space-borne gravitational wave detector, *Class. Quant. Grav.* **33**, 035010 (2016), arXiv:1512.02076 [astro-ph.IM].
- [10] M. Tinto, F. B. Estabrook, and J. Armstrong, Time delay interferometry with moving spacecraft arrays, *Phys. Rev. D* **69**, 082001 (2004), arXiv:gr-qc/0310017.
- [11] D. A. Shaddock, M. Tinto, F. B. Estabrook, and J. Armstrong, Data combinations accounting for LISA spacecraft motion, *Phys. Rev. D* **68**, 061303 (2003), arXiv:gr-qc/0307080.
- [12] G. Wang, Time-delay Interferometry for ASTROD-GW (2011), arXiv:2406.14173 [gr-qc].
- [13] O. Hartwig and M. Muratore, Characterization of time delay interferometry combinations for the LISA instrument noise, *Phys. Rev. D* **105**, 062006 (2022), arXiv:2111.00975 [gr-qc].
- [14] M. Vallisneri, Geometric time delay interferometry, *Phys. Rev. D* **72**, 042003 (2005), [Erratum: *Phys. Rev. D* **76**, 109903(2007)], arXiv:gr-qc/0504145 [gr-qc].
- [15] G. Wang, W.-T. Ni, W.-B. Han, and C.-F. Qiao, Algorithm for time-delay interferometry numerical simulation and sensitivity investigation, *Phys. Rev. D* **103**, 122006 (2021), arXiv:2010.15544 [gr-qc].
- [16] T. A. Prince, M. Tinto, S. L. Larson, and J. W. Armstrong, The LISA optimal sensitivity, *Phys. Rev. D* **66**, 122002 (2002), arXiv:gr-qc/0209039 [gr-qc].
- [17] M. Vallisneri, J. Crowder, and M. Tinto, Sensitivity and parameter-estimation precision for alternate LISA configurations, *Class. Quant. Grav.* **25**, 065005 (2008), arXiv:0710.4369 [gr-qc].
- [18] O. Hartwig, *Instrumental modelling and noise reduction algorithms for the Laser Interferometer Space Antenna*, Ph.D. thesis, Leibniz U., Hannover (2021).
- [19] M. Vallisneri, Synthetic LISA: Simulating time delay interferometry in a model LISA, *Phys. Rev. D* **71**, 022001 (2005), arXiv:gr-qc/0407102 [gr-qc].
- [20] M. Otto, Time-Delay Interferometry Simulations for the Laser Interferometer Space Antenna (2015).
- [21] J.-B. Bayle, M. Lilley, A. Petiteau, and H. Halloin, Effect of filters on the time-delay interferometry residual laser noise for LISA, *Phys. Rev. D* **99**, 084023 (2019), arXiv:1811.01575 [astro-ph.IM].
- [22] M. Muratore, D. Vetrugno, and S. Vitale, Revisitation of time delay interferometry combinations that suppress laser noise in LISA, *Class. Quant. Grav.* **37**, 185019 (2020), arXiv:2001.11221 [astro-ph.IM].
- [23] M. Staab, M. Lilley, J.-B. Bayle, and O. Hartwig, Laser noise residuals in LISA from onboard processing and time-delay interferometry, (2023), arXiv:2306.11774 [astro-ph.IM].
- [24] M. Otto, G. Heinzel, and K. Danzmann, TDI and clock noise removal for the split interferometry configuration of LISA, *Class. Quant. Grav.* **29**, 205003 (2012).
- [25] O. Hartwig and J.-B. Bayle, Clock-jitter reduction in LISA time-delay interferometry combinations, *Phys. Rev. D* **103**, 123027 (2021), arXiv:2005.02430 [astro-ph.IM].
- [26] <https://github.com/gw4gw/LISA-Like-Orbit>.
- [27] G. Wang and W.-T. Ni, Numerical simulation of time delay interferometry for TAIJI and new LISA, *Res. Astron. Astrophys.* **19**, 058 (2019), arXiv:1707.09127 [astro-ph.IM].
- [28] G. Wang and W.-T. Ni, Revisiting time delay interferometry for unequal-arm LISA and TAIJI, *Phys. Scripta* **98**, 075005 (2023), arXiv:2008.05812 [gr-qc].
- [29] D. A. Shaddock, B. Ware, R. E. Spero, and M. Vallisneri, Post-processed time-delay interferometry for LISA, *Phys. Rev. D* **70**, 081101 (2004), arXiv:gr-qc/0406106.
- [30] M. Staab, J.-B. Bayle, O. Hartwig, A. Hees, M. Lilley, G. Woan, and P. Wolf, Optimal design of interpolation methods for time-delay interferometry, (2024), arXiv:2412.14884 [astro-ph.IM].
- [31] O. Hartwig, M. Lilley, M. Muratore, and M. Pironi, Stochastic gravitational wave background reconstruction for a nonequilateral and unequal-noise LISA constellation, *Phys. Rev. D* **107**, 123531 (2023), arXiv:2303.15929 [gr-qc].
- [32] G. Wang, SATDI: Simulation and Analysis for Time-Delay Interferometry, (2024), arXiv:2403.01726 [gr-qc].
- [33] N. Aghanim *et al.* (Planck), Planck 2018 results. VI. Cosmological parameters, *Astron. Astrophys.* **641**, A6 (2020), [Erratum: *Astron. Astrophys.* **652**, C4 (2021)], arXiv:1807.06209 [astro-ph.CO].
- [34] T. P. Robitaille *et al.* (Astropy), Astropy: A Community Python Package for Astronomy, *Astron. Astrophys.* **558**, A33 (2013), arXiv:1307.6212 [astro-ph.IM].
- [35] A. Bohé *et al.*, Improved effective-one-body model of spinning, nonprecessing binary black holes for the era of gravitational-wave astrophysics with advanced detectors, *Phys. Rev. D* **95**, 044028 (2017), arXiv:1611.03703 [gr-qc].
- [36] R. Cotesta, S. Marsat, and M. Pürrer, Frequency domain reduced order model of aligned-spin effective-one-body waveforms with higher-order modes, *Phys. Rev. D* **101**, 124040 (2020), arXiv:2003.12079 [gr-qc].
- [37] M. R. Adams and N. J. Cornish, Discriminating between a Stochastic Gravitational Wave Background and Instrument Noise, *Phys. Rev. D* **82**, 022002 (2010), arXiv:1002.1291 [gr-qc].
- [38] J. D. Romano and N. J. Cornish, Detection methods for stochastic gravitational-wave backgrounds: a

- unified treatment, *Living Rev. Rel.* **20**, 2 (2017), arXiv:1608.06889 [gr-qc].
- [39] F. Feroz, M. P. Hobson, and M. Bridges, MultiNest: an efficient and robust Bayesian inference tool for cosmology and particle physics, *Mon. Not. Roy. Astron. Soc.* **398**, 1601 (2009), arXiv:0809.3437 [astro-ph].
- [40] J. Buchner, A. Georgakakis, K. Nandra, L. Hsu, C. Rangel, M. Brightman, A. Merloni, M. Salvato, J. Donley, and D. Kocevski, X-ray spectral modelling of the AGN obscuring region in the CDFS: Bayesian model selection and catalogue, *Astron. Astrophys.* **564**, A125 (2014), arXiv:1402.0004 [astro-ph.HE].
- [41] C. García-Quirós, S. Tiwari, and S. Babak, GPU-accelerated LISA parameter estimation with full time domain response, (2025), arXiv:2501.08261 [gr-qc].
- [42] G. Wang, (2025), in Preparation.
- [43] C. R. Harris, K. J. Millman, S. J. van der Walt, R. Gommers, P. Virtanen, D. Cournapeau, E. Wieser, J. Taylor, S. Berg, N. J. Smith, R. Kern, M. Picus, S. Hoyer, M. H. van Kerkwijk, M. Brett, A. Haldane, J. F. del Río, M. Wiebe, P. Peterson, P. Gérard-Marchant, K. Sheppard, T. Reddy, W. Weckesser, H. Abbasi, C. Gohlke, and T. E. Oliphant, *Array programming with NumPy*, *Nature* **585**, 357 (2020).
- [44] P. Virtanen, R. Gommers, T. E. Oliphant, M. Haberland, T. Reddy, D. Cournapeau, E. Burovski, P. Peterson, W. Weckesser, J. Bright, S. J. van der Walt, M. Brett, J. Wilson, K. J. Millman, N. Mayorov, A. R. J. Nelson, E. Jones, R. Kern, E. Larson, C. J. Carey, Í. Polat, Y. Feng, E. W. Moore, J. VanderPlas, D. Laxalde, J. Perktold, R. Cimrman, I. Henriksen, E. A. Quintero, C. R. Harris, A. M. Archibald, A. H. Ribeiro, F. Pedregosa, P. van Mulbregt, and SciPy 1.0 Contributors, SciPy 1.0: Fundamental Algorithms for Scientific Computing in Python, *Nature Methods* **17**, 261 (2020).
- [45] T. pandas development team, pandas-dev/pandas: Pandas (2020).
- [46] J. D. Hunter, Matplotlib: A 2D Graphics Environment, *Comput. Sci. Eng.* **9**, 90 (2007).
- [47] A. Lewis, GetDist: a Python package for analysing Monte Carlo samples, (2019), arXiv:1910.13970 [astro-ph.IM].
- [48] J.-B. Bayle and O. Hartwig, Unified model for the LISA measurements and instrument simulations, *Phys. Rev. D* **107**, 083019 (2023), arXiv:2212.05351 [gr-qc].